Rapid and automated multidimensional fluorescence microscopy profiling of 3D human breast cultures

Catherine C. Park[a,b*], Walter Georgescu[a], Aris Polyzos[a], Christopher Pham[a], Kazi M. Ahmed[ab], Hui Zhang[a], Sylvain V. Costes[a*]

a. Life Sciences Division, Lawrence Berkeley National Laboratory, Berkeley, CA 94720 USA

b. Department of Radiation Oncology, University of California, San Francisco, CA

** Co-corresponding authors*

Abstract

Three-dimensional (3D) tissue culture provides a physiologically relevant microenvironment for distinguishing malignant from non-malignant breast cell phenotypes. 3D culture assays can also be used to test novel cancer therapies and predict a differential response to radiation between normal and malignant cells in vivo. However, biological measurements in such complex models are difficult to quantify and current approaches do not allow for in-depth multifaceted assessment of individual colonies or unique sub-populations within the entire culture. This is in part due to the limitations of imaging at a range of depths in 3D culture resulting from optical aberrations and intensity attenuation. Here, we address these limitations by combining sample smearing techniques with high-throughput 2D imaging algorithms to accurately and rapidly quantify imaging features acquired from 3D cultures. Multiple high resolution imaging features especially designed to characterize 3D cultures show that non-malignant human breast cells surviving large doses of ionizing radiation acquire a ''swelled acinar'' phenotype with fewer and larger nuclei, loss of cell connectivity and diffused basement membrane. When integrating these imaging features into hierarchical clustering classification, we could also identify subpopulations of phenotypes from individual human tumor colonies treated with ionizing radiation or/and integrin inhibitors. Such tools have therefore the potential to further characterize cell culture populations after cancer treatment and identify novel phenotypes of resistance.

Introduction

Histologically, heterogeneity within individual cancers has long been recognized, however its relevance is just beginning to be addressed. The advent of 3D cell cultures which facilitates recapitulation of morphogenesis that occurs *in vivo* has allowed us to observe a larger range of this heterogeneity in the laboratory. It is well accepted that 3D tissue culture emulates the normal physiologic microenvironment more closely than traditional 2-dimensional techniques, and can more readily replicate morphologies observed *in vivo*[1]. In 3D laminin-rich extracellular matrix culture (lrECM), non-malignant human mammary epithelial cells (HMEC) form organotypic 'acinar' structures

that resemble the secretory alveoli observed in the mammary gland *in vivo*[2], while malignant cells form highly disorganized colonies with disrupted cell-ECM interactions [3, 4]. In particular, we have previously shown that 3D lrECM culture assay rapidly distinguishes response of normal and malignant colonies to ionizing radiation (IR) and therapeutic inhibition of β1 integrins. We also showed in this study that response in 3D lrECM is highly predictive of responses seen *in vivo* [5]. Therefore, the use of 3D lrECM is both relevant and necessary for improved modeling of normal and malignant cells, and to quantify the heterogeneity in these populations following treatment.

Comprehensive high-throughput analysis of multiple features of single colonies in a complete 3D lrECM population has not been feasible to date. We have relied on time-consuming manual counting techniques to analyze a single fluorophore at a time. In addition, images taken at high magnification views to highlight a specific feature may not capture representative populations present in the culture. In this work, we present a solution for allowing rapid and accurate quantification of multiple morphologic and immunofluorescence-detected features in 3D cell cultures simultaneously. We combined a technique of simple culture preparation to optimize signal and reduce background across ~100 μm thick specimens, allowing use of conventional 2D microscopy [1]. Low magnification objectives were then used with high numerical aperture to reduce imaging to one focal plane without affecting spatial resolution, while also permitting the sampling of an entire culture. The integration of these methods with novel and existing imaging algorithms resulted in high content analysis of large numbers of individual acini that were characterized for simple morphologic features (size, shape) and biologic endpoints (apoptosis, proliferation). In addition, spatial distribution of molecules such as β1 and α6 integrins that critically signal between cells and extracellular matrix could be evaluated in individual colonies in depth. By applying these advanced imaging and image processing techniques to classical biological endpoints we created a 14-feature profile. We applied this profile to tumor colonies treated with IR or integrin inhibitors, identifying phenotypes unique to each of these treatments. The ability to characterize and quantify previously indistinguishable subpopulations that survive radiation indicates that heterogeneity is a critical factor to consider in modeling treatment response, and can lead to identification of novel mechanisms of resistance.

Materials and Methods

Cell culture: Human mammary epithelial (HMECs) cells MCF10A and malignant breast cells, HMT-3522 T4-2, were maintained according to the published protocols[6]. MCF10A cells were grown in DMEM-F12 supplemented with 5% horse serum, 0.02ug/ml of EGF, 10ug/ml of insulin, 0.5ug/ml of hydrocortisone, 0.1ug/ml of cholera toxin, and 1X penicillin/streptomycin. T4-2 cells were grown in DMEM-F12 medium with 0.25ug/ml of insulin, 10ug/ml of transferrin, 2.6ng/ml of sodium selenite, 1.4×10^{-6}M of hydrocortisone, 10^{-10}M of estradiol and 5μg/ml of prolactin. Cells were maintained at 37ºC and 5% CO2. The culture medium was replaced every 3 days.

For on-top 3-dimensional lrECM cell culture, a 12mm diameter round coverslip overlaid with ~1 mm (125μL) of lrECM was placed at the bottom of each well of 24-well plates. Cells were then plated at a density of 3×10^4 cells/cm^2 in growth medium supplemented

with 5% v/v laminin-rich extra-cellular matrix (lrECM) (BD Biosciences, San Jose, California). The culture was maintained at 37ºC and 5% CO2.

Radiation: Ionizing radiation was delivered using a CP160 Faxitron (160 KV) X-ray irradiator at a dose-rate of 1 Gy/min for a total dose of 8 Gy, or sham-irradiated.

Immunofluorescence: At the appropriate time point, coverslips were fixed by washing with PBS followed by incubation at -10ºC for 1 hr immersed in cold methanol:acetone (1:1). The coverslips were subsequently washed with PBS, and immersed in blocking solution composed of 10% v/v goat serum, 8 µg/mL goat anti-mouse IgG (Caltag #435000) and IF buffer (0.5 g/L NaN3, 0.1% BSA, 0.2% Triton X-100, 0.05% Tween-20) and incubated at 4ºC overnight. Coverslips were then inverted onto 20 µL of primary antibodies in 10% goat serum in IF buffer and incubated at 4ºC overnight. Primary antibodies used were (i) rabbit anti-β1-integrin (Abcam #16667) (at 1:50 dilution) and (ii) rat anti-α6-integrin (Millipore #MAB 1378) (at 1:300 dilution). Coverslips were washed with IF buffer (3x 20min) and incubated with secondary antibody at 4ºC overnight. Secondary antibodies used were (i) donkey anti-rabbit IgG Alexa 594 (Invitrogen) (at 1:200 dilution) and (ii) goat anti-rat IgG Alexa 488 (Invitrogen) (at 1:200 dilution). Acini were subsequently washed with IF buffer (3x 1hr) and coated with vectashield (Vector labs) prior to being mounted onto glass slides, sealed with nail polish and then stored at 4ºC until imaging.

Image acquisition, processing and analysis: Cells were viewed and imaged using a Zeiss Axio Observer Z1 automated microscope (Carl Zeiss, Jena, Germany). In order to acquire a large amount of specimen, maximizing acquisition time and simplifying analysis, a full scan of a slide was first done with a low magnification objective (5X) using DAPI and the "Mosaix" module of Axiovision. A full 2 cm x 4 cm slide is typically scanned within 5 min. For the low magnification scan, no autofocus function was used. Instead, Z positions were entered manually for the corner and center positions of the slide. "Mosaix" uses interpolation schemes to determine Z positions for the rest of the slide. If too many positions are out of focus, more Z positions are entered in the module and the slide is scanned one more time. The resulting image montage was analyzed automatically by an external Java routine to identify where colonies are present. Then, the routine generates a list of positions fed back to the "Mark and Find" module of Axiovision. High resolution images were acquired for each of these positions using a high NA Zeiss plan-apochromat 20X (NA of 0.8), a sensitive scientific-grade EM-CCD camera (Axiocam) with autofocus "on" for Z position refinement. Imaging each position takes about 5 sec and no more than a thousand images are taken per slide. Images are saved on a server and a fully automated script generates acinus segmentation and individual acini measurements described in this manuscript. For comparison to confocal images, Z-stacks were taken with a 5 µm step width and a 40X (NA of 0.95). Each treatment considered in the manuscript led to 100 to 1000 acini in 3 to 4 individual experiments. Image processing was performed using Matlab (MathWorks Inc, Natick, MA) and DIPimage (image processing toolbox for Matlab, Delft University of Technology, The Netherlands). *Statistical analysis:* To compute the various statistical tests described in the text, as well as hierarchical clustering and radial intensity interpolation we used the statistic toolbox in Matlab and the R statistical computing environment (http://www.r-project.org).

Results

Rapid 2D image screening reveals accurate 3D properties of acini in a high-throughput manner.

We previously developed a simple technique to sample an entire 3D culture in a 2D format [1]. As depicted in Supplemental Figure S1, the 3D cell culture contents are gently smeared across a standard glass slide, allowing optimal immunofluorescence imaging.

Here, we developed a series of computer scripts to increase the throughput of 3D cell analysis, based on automated 2D image acquisition of comprehensive fields of view from slides prepared with the smearing technique. To automatically identify individual acini in each field of view, isodata local thresholding [7] of integrin immunostaining followed by a watershed algorithm was used. Touching acini could also be separated manually by a semi-automated tool (Fig. S1). All intensity measurements described below assume background subtraction. Background was computed as the mean intensity in areas where no acini were detected. To establish a quantitative algorithm for assessing the number of nuclei per acinus, we applied an intensity-based signal separation algorithm we developed previously [8, 9]. Briefly, total DAPI intensity within a single acinus is divided by the mean total intensity measured for individual nuclei (colored nuclei in Fig. 1A - identified automatically based on shape and size). The approach is summarized in equation 1:

$$num_nuc = \frac{\sum_{i,j \in nuc_mask} I_{nuc}(i,j)}{\left\langle \sum_{i,j, \in isolated\ nucleus} I_{nuc(i,j)} \right\rangle}, \qquad (1)$$

where *num_nuc* is the number of nuclei for a given acinus, $I_{nuc}(i,j)$ is the intensity for pixel (i,j) in the nuclear channel DAPI and the brackets < > indicate average over all isolated nuclei identified in a field of view. In order to validate the quantification performed on 2D images, we compared nuclear counts for 150 acini acquired either by confocal microscope or by 2D conventional microscopy. Normal acini have more densely packed cells, making quantification more difficult. Therefore, we used normal acini to validate the approach as the worst-case scenario. Acini were selected from different culture wells after various times in culture to sample over a large size variation. Smearing the cultures led to very similar imaging conditions across various acini sizes, with essentially two layers of cells packed against each other (Fig. 1C and 1E). Confocal 3D stacks were used to manually count each individual nuclei. 2D images were used to estimate the number of nuclei semi-automatically after identifying isolated nuclei in each field of view (information necessary to compute denominator in equation 1). Fig. 1D displays two panels showing the log of the ratio between both counts and the 2D estimated counts as a function of 3D manual counts (i.e.true values).The overall results show high correlation between the 2D and true counts (R^2=0.93) with 95% of the counts being within 50% of the manual count values (red dotted lines - Fig. 1D)

High-content analysis of acinar properties reveals quantifiable morphologic features after exposure to IR

Manual counting of nuclei and acinar size has previously demonstrated that targeted treatment and radiation lead to emergence of distinct subpopulations within the culture [10, 11]. However, the ability to perform in-depth analysis of these subpopulations

manually has been limited and 3D quantification in general is challenging [12]. We performed high-content automated analysis of multiple parameters to characterize a population of HMEC's that survived 8 Gy of IR versus IR sham (representative images in Fig. 2A). Fully-grown acini were first exposed to IR or IR sham treatment, before acini were disaggregated and expanded as monolayer to simulate long period of time following exposure *in vivo*. After one full passage, surviving cells were grown back into 3D for 10 days and colonies were scored with our imaging approach.

To characterize morphologic features of individual acini in a population, we first plotted the number of nuclei per acinus as a function of individual acinar size (Fig. 2B). The acinar area was estimated by the number of pixels comprised in the acinus mask, defined automatically by isodata thresholding [7] of alpha-6 integrin immunofluorescence signal. This distribution revealed a difference between the irradiated and sham-treated populations showing distinct scatterplot for both treatments. There were significantly more small acini in the irradiated group and fewer nuclei per acinus. Individual distributions were compared with the Kolmogorov-Smirnov statistical test (KS-test) leading to highly significant P-values. Interestingly, as clearly observable in Fig. 2A, one reason for so fewer nuclei per acinus in the irradiated group was the fact that individual nuclei were much larger.

To further characterize the difference between both treatments, the nuclear density (number of nuclei per unit acini area - nuclei/μm^2) was assessed for each acinus and plotted according to frequency (Fig 2C). The distribution strikingly revealed a much higher nuclear density for normal acini peaking at 6.4×10^{-3} nuclei/μm^2 against 3.8×10^{-3} nuclei/μm^2 after IR ($P_{ks}<0.001$). In order to determine whether radiation had a global effect on the ability of exposed cells to form normal polarized structures, we also measured how spherical these structures were. This was done by computing the normalized compactness (*C*) also called spherical index [9]. Briefly, *C* is defined for a 2D object as:

$$C = \frac{P^2}{4\pi A} \qquad (2)$$

where *A* is the area of the object and *P* is its perimeter. According to the isoperimetric inequality, the numerator of this ratio is greater than the denominator except in the case of a circle where the two values are equal. Therefore, *C* is equal to 1 for a perfectly circular acinus and it increases as the acinus becomes more deformed. As we previously reported [9], normal acini have a narrow distribution for their compactness with a peak centered around 1.15 (Fig. 2D). In contrast, the irradiated population showed a much broader distribution with 45% of the acini having a *C* value above 1.85. The difference between the two distributions was highly significant as well.

Together, these measurements provide a quantitative analysis of morphologic features of the cells that have survived 8 Gy irradiation. This more in-depth characterization revealed a phenotype that has increased numbers of smaller colonies, decreased nuclear density and more deformed structures.

Average concentric radial intensity (ACRI) profiles reveal altered patterns of integrin expression in HMEC colonies surviving 8 Gy IR

The presence of extracellular matrix dramatically alters cell response to IR [13-16]. The

use of 3D lrECM culture allows us to interrogate the role of ECM in IR response in more depth. We have previously seen evidence for altered redistribution of basement membrane proteins in irradiated HMEC's [17], or in mammary glands of mice exposed to high LET IR [18]. However, it is not clear how global this phenomenon in the progeny of irradiated cells, or whether there is a distinctive pattern after IR. In addition, the presence of a lumen, which is another characteristic of a normal acinus, is not an easy feature to quantify [9]. In order to address these challenges in quantification, we used a very simple yet elegant imaging method to determine a one-dimensional (1D) radial intensity profile of the integrin staining. As previously described, once the binary mask of the acinus is obtained, one can manipulate such a mask to derive other information. To obtain the radial distribution of the intensity profile for any staining located inside an acinus, one can first compute the distance-transform of the mask [19] which can then be rounded to obtain a series of isocontours of equal radial distance from the geometric center. These isocontours can then be used to compute the mean intensity of any signal such as the integrin α6 (Fig. 3A). Analogous to "peeling an onion", the result is a 1D radial intensity profile that measures the integrin distribution throughout the acinus. The radial intensity profile can be used to identify the acinar edge where the basal cells contact the extracellular matrix. The method is further described in supplemental figure Fig. S2. Briefly, one can notice from the DAPI profile that DNA density is highest in the center of the acinus and fairly flat inside the acinus (Fig. S2D). The acinus boundary is defined by the full width half max of DAPI signal on the edge of the mask and coincides well with the peak observed in the radial profile of α6 integrin (Fig. S2E), which is slightly outside the nuclear boundary of basal cells as one would expect for a normal acinus.

This method was applied to determine the average radial intensity profile of DAPI and α6 integrin across multiple acini in a population (representative images shown in Fig. 3B and 3C, respectively). We interpolated the radial profiles of thousands of acini for three different experiments to an average radius of 50 pixels (30 μm radius). Average profiles for three different experiments are plotted after normalizing intensities to the maximum intensity for the stain (Fig. 3D,E). By scaling intensities this way, one can better visualize the spatial integrin redistribution that takes place in HMEC surviving 8 Gy of IR. For α6 integrin we observed an increase in the overall intensity levels coupled to a flattening of the intensity profile for the irradiated acini when compared with non-irradiated controls. These changes reflect the loss of polarization and disorganization that occurs in the irradiated acini. We also observed a decrease in the DAPI intensity levels for the irradiated acini, which reflects the decreased number of cells present in irradiated acini (Fig. 2C). The DAPI intensity profile is again flattened when compared to control acini reflecting a decrease in organization in the irradiated acini. In order to reflect spatial distribution independently of acinar size, we proposed a simpler metric: the ratio of the mean intensity of the signal for two concentric regions (i.e. ring_ratio). The mean intensity of the inside of the acinus (inner disk) is divided by mean intensity of the outer ring (Fig. S2 C-E). A value greater than 1 indicates a distribution of fluorophore predominantly inside the acinus (e.g. DAPI ratio is 2.2 in Fig. S2D) whereas a value less than 1 indicates a distribution of the fluorophore predominantly on the periphery of the acinus (e.g. α6 ratio is 0.5 in Fig. S2E).

Skeletonization reveals redistribution of integrins at cell-cell junctions within acini following IR exposure

We have previously shown that redistribution of integrins may occur following exposure to IR[17]. However, much of these data remain qualitative in nature. The ACRI algorithm can be used to detect changes in radial distribution of integrins, however, other critical aspects of integrin biology, such as its role in cell-cell interactions can also be further quantitated (Fig. 4A). The linear distribution of integrins between cells could be identified using isodata thresholding as previously introduced. However, thresholding alone leads to segments of various thicknesses. In order to reduce this mask into single pixel lines, we used a classic morphological image processing method, skeletonization [20], which can identify the path of maximum intensity in a grayscale image within a given mask. Location of sharp boundaries at the cell-cell interfaces delimited by β1 integrin immunostaining is well detected with such approach in the non-irradiated group (Fig. 4A). On the other hand, the 8 Gy IR treatment group showed the majority of the skeletonization limited to the periphery of the acinus (Fig. 4B). Resulting boundaries (skeletons) were then used to compute the total intensity of β1 integrin signal (i.e. intensity integrated along path). Note that even though total β1 integrin levels remain similar in the 8 Gy IR treated acini by Western (Fig. 4C,D), the amount located at the intercellular boundary is 50% lower. These results reflect a delocalization of the integrin from a clear linear pattern to a diffuse pattern. Such changes could not be detected by simple western quantification or overall intensity measurement across the acinus, highlighting the power of this technique.

Hierarchical clustering of multiple imaging features identify specific treatment phenotypes

We wished to integrate several individual imaging features to determine whether specific profiles could distinguish different therapies for each acinus or colony. We compared imaging features from four different treatments that are of interest in our laboratories (4 Gy IR, with or without β1 integrin inhibitory antibody, AIIB2). Acini after treatment were labeled simultaneously for integrins (α6 and β1), cell death (caspase-3) and nuclear stain (DAPI). Imaging features introduced in the previous sections (e.g. colony size, compactness, nuclear density, apoptosis, β1 integrin skeletonization, α6 integrin ring ratio) were used to compute 14 features, which defined the imaging profile for each acinus. We normalized each feature across all acini so that the mean for each feature is 0 and the standard deviation is 1. This is a standard procedure necessary to avoid having one feature carrying more weight than others. This resulted in a unique profile for each acinus (Fig. S3). However, when looking across profiles for individual acini (rows), no clear difference could be observed between the four treatments. Therefore, to identify phenotypes with specific combinations of features, we applied hierarchical clustering across all 1034 acini independently of treatment (Fig. 5). Hierarchical clustering was performed with the bioinformatics toolbox of Matlab (Mathworks) and was based on the Euclidean distance between different row profiles, grouping together acini with similar profile (small distance). Using the "furthest neighbor" algorithm to link each row into clusters one can identify distinct clusters distributed among the different treatments. To

avoid having too many small clusters, we used the following approach to determine the distance threshold used for clustering. The minimum distance between clusters was reduced stepwise until any of the resulting clusters were comprised of less than 1% of all the acini (i.e. ~10 acini). This resulted in only nine clusters. Each cluster characterizes a specific phenotype with all acini in this cluster sharing common imaging features referred as "signature". Chi-square test led to significant dependence between the four treatment groups and the nine identified phenotypes ($P<0.001$).

To identify which phenotypes were strongly correlated to specific treatments, we compared the proportion of all phenotypes among each treatment with that expected from random distribution (Fig. 6A). We found that phenotype 4 is poorly correlated to any specific treatment, but rather represented a similar proportion, ~45% of all acini in each treatment. Remaining phenotypes highly specific to one treatment were identifiedwith a proportion greater than 2 standard deviations above the average proportion across all treatments. This led to the identification of five phenotypes representing 10% of the original 1034 acini (Fig. 6B - underscored phenotypes 2, 3, 7, 8, 9). The signatures for these five phenotypes are plotted in Fig. 6C. Interestingly, IR alone showed a strong enrichment for many of these phenotypes (phenotype 2,7 and 9). All of these phenotypes were already present in the control as minorities whereas phenotype 3 remains strong across both control and IR. AIIB2 treatment was highly enriched with Phenotype 8, whereas combined treatment of IR and AIIB2 did not reveal any distinct phenotypes, suggesting additive properties of radiation and AIIB2.

Discussion

Three-dimensional culture models have now superseded the use of traditional 2D tissue culture plastic as a more physiologically relevant representative of the *in vivo* milieu. In addition, as a large body of work has demonstrated, 3D human cell culture better predicts the *in vivo* human response to various treatments than classic monolayer cultures [2, 3, 6, 21-24]. Furthermore, 3D culture models allow for investigation of complex cell-cell and cell-extracellular matrix interactions, morphogenesis, and the context of tissue-like microenvironment. These features are ever more important to quantify and understand as pathologists have been recognizing for decades that human tumors are complex and often comprised of a heterogeneous populations of cells. However, morphologic features and biologic and biochemical measurements are much more challenging to quantify in the 3D culture format due to several limiting factors.

Two main issues are centered around imaging modalities. 1. One needs to comprehensively and rapidly sample the culture; 2. images must have resolutions high enough to quantitate detailed features with biological relevance. Addressing the first issue, recent work used scanning phase images of acini of various breast cell lines and correlated basic morphological features to their gene expression profiles [25]. This approach led to the identification of too few phenotypes as colony characteristics only included gross morphological classification and did not use any protein markers,. We

had previously introduced imaging algorithms that characterize lumen formation and acinar shape [9] but left unexplored the challenges of measuring a array of diverse acinar properties over large populations of acini. Another limiting factor for such exploration was the need of time consuming and storage limited confocal microscopy or light tomography [26].

The approach presented here allows rapid comprehensive quantitation of multiple features of individual colonies within an entire culture population. By smearing the culture contents onto a slide, the specimen depth varies between 20 and 30 μm. This allows the imaging of acini of clonal origins (colonies) without the difficulty of imaging acini located at different depths. In contrast, when imaging through thick Matrigel™ (~100 μm thickness), different depths lead to large variation in imaging quality due to optical aberrations and intensity attenuation. Based on the work we present here, conventional 2D images are clearly sufficient to measure three-dimensional microscopic information.

Multi epitope ligand cell technology has been introduced in the past as a way to identify cells with a unique combination of cell markers [27]. Briefly, this technology consists of directly labeling and consecutively imaging tens to hundreds of proteins in the same field of view. This produces a vector consisting of the different protein levels measured in individual cells. Specific cell types are believed to have very distinct and unique combinations of protein levels and a combinatorial approach can then be applied to identify these various types. This approach was recently combined with hierarchical clustering to identify stem cells in human skin specimens[28]. In our work, we used a similar concept, but applied it to a set of imaging features from protein markers intensity. In addition, we modified the approach in two key ways that are more relevant to the 3D format: 1. we applied it at the acinar level instead of the cellular level. 2. to have more statistical power for separating acinar phenotypes, we also increased the size of the vector by adding imaging features important for describing acinar cultures such as cell-cell adhesion, basement membrane integrity, nuclear density, and acini morphology. Surprisingly, when applying this technology to breast cells in 3D lrECM [29], each acinus shows quite a unique imaging profile even within the same treatment. This heterogeneity dominates to the extent that no obvious combination of features clearly separates different treatments. However, applying hierarchical clustering across all acini, independently of treatment, shows that the response to β1 inhibitor or IR seems to be driven by a subgroup of acini (10% of all acini), responding very differently to each treatment. This is in stark contrast to the classical view and expectation of a homogenous population response. Such quantitative approaches increase our opportunity to accurately identify and investigate specific phenotypes observed after exposure to IR [30], or drug resistance observed after chemotherapeutic or kinase inhibitor treatments [31].

In terms of the biological response characterized in this work, our results indicate that non-malignant HMEC surviving large doses of IR have radically changed their morphology, acquiring a phenotype similar to breast cancer cells [32]. We are now able to quantitate this phenomenon with a higher degree of accuracy and reproducibility. This result is interesting in light of our previous findings that HMECs irradiated with 2 Gy IR

undergo epithelial-to-mesenchymal transition (EMT)[11]. We also previously showed by confocal microscopy that radiation alone could lead to disrupted cell-cell communication, aberrant cell-extracellular matrix interactions, and loss of tissue-specific architecture [17]. In the work presented here, however, our results take us further in characterizing this neoplastic progression by identifying precisely the morphological changes that are taking place. We show that the progeny of HMEC surviving 8 Gy of IR seem to have a "swelled morphological phenotype", with fewer and more dispersed nuclei inside the acinus. This change seems to be correlated with a loss of anchorage of basal proteins such as α6 integrins, which are redistributed, and diffusively filling the acinus. Such basal signal inside the acinus probably leads to the loss of polarization observed in the 8 Gy group, and basal cells lose their organization cues by receiving basal signal from all directions. Interestingly, α6 is only slightly increased in the basement membrane. Also, as previously observed for E-cadherin, cells have lost their self-adhesion properties, as β1 integrin signals, even though overall amounts are unchanged, are now relocalized at the basement membrane.

Finally, our work addresses the importance of recognizing heterogeneity of tumor response to treatment. It has long been recognized that tumors do not uniformly respond to therapy, and that as therapy is administered, the populations that remain and survive may have acquired properties of resistance. To date, it has been challenging to capture and quantify such treatment related heterogeneity, and it remains unclear what the significance of such heterogeneity is. However, a critical step in understanding the nature and relevance of the cells that survive treatment is to characterize and reproducibly quantify their features. Our work suggests that the majority of the cancer cell population responds uniformly to treatment, however, 10% of the population acquires characteristics that are limited to specific features. These heretofore unrecognized subpopulations may form the basis for understanding the emergence of resistance, and the heterogeneity of populations that may not respond similarly to the same therapy administered over time. This may have profound implications for the tailoring and paradigm of targeted therapy.

Acknowledgement

This project was mainly supported by a R01 ARRA grant from NIH [CA124891]. SVC and WG were additionally supported by the Low Dose Scientific Focus Area, United States Department of Energy [DE-AC02-05CH11231] by the ICBP program of NCI [U54CA149233]. The content is solely the responsibility of the authors and does not necessarily represent the official views of the National Cancer Institute, the National Institutes of Health or the Department of Energy.

References

1. Park, C.C., et al., *Beta1 integrin inhibitory antibody induces apoptosis of breast cancer cells, inhibits growth, and distinguishes malignant from normal phenotype in three dimensional cultures and in vivo.* Cancer Res, 2006. **66**(3): p. 1526-35.
2. Barcellos-Hoff, M.H., et al., *Functional differentiation and alveolar morphogenesis of primary mammary cultures on reconstituted basement membrane.* Development, 1989. **105**(2): p. 223-35.
3. Debnath, J. and J.S. Brugge, *Modelling glandular epithelial cancers in three-dimensional cultures.* Nat Rev Cancer, 2005. **5**(9): p. 675-88.
4. Weaver, V.M., et al., *The importance of the microenvironment in breast cancer progression: recapitulation of mammary tumorigenesis using a unique human mammary epithelial cell model and a three-dimensional culture assay.* Biochem Cell Biol, 1996. **74**(6): p. 833-51.
5. Park, C.C., et al., *Beta1 integrin inhibition dramatically enhances radiotherapy efficacy in human breast cancer xenografts.* Cancer Res, 2008. **68**(11): p. 4398-405.
6. Debnath, J., S.K. Muthuswamy, and J.S. Brugge, *Morphogenesis and oncogenesis of MCF-10A mammary epithelial acini grown in three-dimensional basement membrane cultures.* Methods, 2003. **30**(3): p. 256-68.
7. Ridler, T. and S. Calvard, *Picture threshholding using an iterative selection method.* IEEE Trans on Systems, Man, and Cybernetics., 1978. **SMC-8**(8): p. 630-2.
8. Fleisch, M.C., et al., *Intensity-based signal separation algorithm for accurate quantification of clustered centrosomes in tissue sections.* Microsc Res Tech, 2006. **69**(12): p. 964-72.
9. Tang, J., et al., *Phenotypic transition maps of 3D breast acini obtained by imaging-guided agent-based modeling.* Integr Biol (Camb), 2011. **3**(4): p. 408-21.
10. Andarawewa, K.L., et al., *Lack of radiation dose or quality dependence of epithelial-to-mesenchymal transition (EMT) mediated by transforming growth factor beta.* Int J Radiat Oncol Biol Phys, 2011. **79**(5): p. 1523-31.
11. Andarawewa, K.L., et al., *Ionizing radiation predisposes nonmalignant human mammary epithelial cells to undergo transforming growth factor beta induced epithelial to mesenchymal transition.* Cancer Res, 2007. **67**(18): p. 8662-70.
12. Ng, K.W., D.T. Leong, and D.W. Hutmacher, *The challenge to measure cell proliferation in two and three dimensions.* Tissue Eng, 2005. **11**(1-2): p. 182-91.
13. Damiano, J.S., L.A. Hazlehurst, and W.S. Dalton, *Cell adhesion-mediated drug resistance (CAM-DR) protects the K562 chronic myelogenous leukemia cell line from apoptosis induced by BCR/ABL inhibition, cytotoxic drugs, and gamma-irradiation.* Leukemia : official journal of the Leukemia Society of America, Leukemia Research Fund, U.K, 2001. **15**(8): p. 1232-9.
14. Cordes, N., *Integrin-mediated cell-matrix interactions for prosurvival and antiapoptotic signaling after genotoxic injury.* Cancer letters, 2006. **242**(1): p. 11-9.
15. Cordes, N. and C. Beinke, *Fibronectin alters cell survival and intracellular signaling of confluent A549 cultures after irradiation.* Cancer biology & therapy, 2004. **3**(1): p. 47-53.

16. Cordes, N., et al., *Fibronectin and laminin increase resistance to ionizing radiation and the cytotoxic drug Ukrain in human tumour and normal cells in vitro.* International journal of radiation biology, 2003. **79**(9): p. 709-20.
17. Park, C.C., et al., *Ionizing radiation induces heritable disruption of epithelial cell interactions.* Proc Natl Acad Sci U S A, 2003. **100**(19): p. 10728-33.
18. Costes, S., C.H. Streuli, and M.H. Barcellos-Hoff, *Quantitative image analysis of laminin immunoreactivity in skin basement membrane irradiated with 1 GeV/nucleon iron particles.* Radiat Res, 2000. **154**(4): p. 389-97.
19. Knowles, D.W., et al., *Automated local bright feature image analysis of nuclear protein distribution identifies changes in tissue phenotype.* Proc Natl Acad Sci U S A, 2006. **103**(12): p. 4445-50.
20. Serra, J., *[Biomedical image analysis by mathematical morphology (author's transl)].* Pathol Biol (Paris), 1979. **27**(4): p. 205-7.
21. Gudjonsson, T., et al., *To create the correct microenvironment: three-dimensional heterotypic collagen assays for human breast epithelial morphogenesis and neoplasia.* Methods, 2003. **30**(3): p. 247-55.
22. Andrei, G., *Three-dimensional culture models for human viral diseases and antiviral drug development.* Antiviral Res, 2006. **71**(2-3): p. 96-107.
23. Pickl, M. and C.H. Ries, *Comparison of 3D and 2D tumor models reveals enhanced HER2 activation in 3D associated with an increased response to trastuzumab.* Oncogene, 2009. **28**(3): p. 461-8.
24. Harma, V., et al., *A comprehensive panel of three-dimensional models for studies of prostate cancer growth, invasion and drug responses.* PLoS One, 2011. **5**(5): p. e10431.
25. Han, J., et al., *Molecular predictors of 3D morphogenesis by breast cancer cell lines in 3D culture.* PLoS Comput Biol, 2011. **6**(2): p. e1000684.
26. Thurner, P., et al., *3D morphology of cell cultures: a quantitative approach using micrometer synchrotron light tomography.* Microsc Res Tech, 2005. **66**(6): p. 289-98.
27. Schubert, W., et al., *Analyzing proteome topology and function by automated multidimensional fluorescence microscopy.* Nat Biotechnol, 2006. **24**(10): p. 1270-8.
28. Ruetze, M., et al., *In situ localization of epidermal stem cells using a novel multi epitope ligand cartography approach.* Integr Biol (Camb), 2011. **2**(5-6): p. 241-9.
29. Weaver, V.M., et al., *The development of a functionally relevant cell culture model of progressive human breast cancer.* Semin Cancer Biol, 1995. **6**(3): p. 175-84.
30. Mukhopadhyay, R., et al., *Promotion of variant human mammary epithelial cell outgrowth by ionizing radiation: an agent-based model supported by in vitro studies.* Breast Cancer Res, 2010. **12**(1): p. R11.
31. Huang, C., et al., *beta1 integrin mediates an alternative survival pathway in breast cancer cells resistant to lapatinib.* Breast Cancer Res, 2011. **13**(4): p. R84.
32. Howlett, A.R., et al., *Cellular growth and survival are mediated by beta 1 integrins in normal human breast epithelium but not in breast carcinoma.* J Cell Sci, 1995. **108 (Pt 5)**: p. 1945-57.

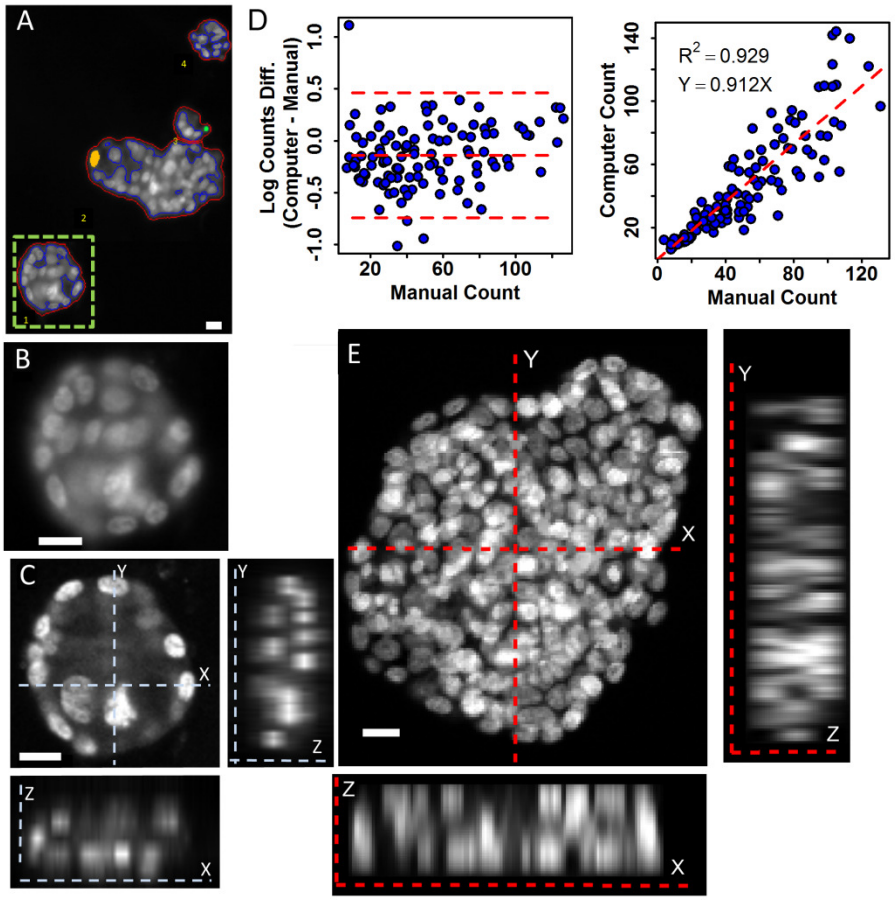

Fig. 1. Automated cell counting algorithm validated by 3-dimensional confocal microscopy. (A) Snapshot of acini analysis. In-house automated computer algorithms produce an image showing each normal acinar colony contour in red overlaid with a contour of nuclei stained by DAPI in blue. An identification number is assigned for each acinus (labeled at left-bottom of the acinus). To count the number of nuclei in each colony, the total DAPI intensity of all nuclei (blue contour) is divided by the average DAPI intensity of the single nucleus (see Eq. 1). Isolated nuclei are identified and labeled (here, shown in green and yellow, scale bars =15 µm). (B) A high-powered magnification view of acinus number 1 from panel A (inside green dash box in A) is shown. (C) The corresponding 3-dimensional image of the same acinus acquired by confocal microscopy (40 slices, with 0.75 µm interval, acquired in 5 min) is shown. (D) Differences of the logarithmic counts (dotted lines indicate means and 95% confidence interval) and linear regression analysis (based on 150 acini) comparing quantitation of nuclei using 2D images versus manual counts obtained from 3D confocal z-stacks. Results indicate 2D automatic counts may be substituted for 3D manual counts . (E) 3D confocal image of a larger acini, showing the smearing techniques flattens large structures enough to allow accurate quantification of nuclei number.

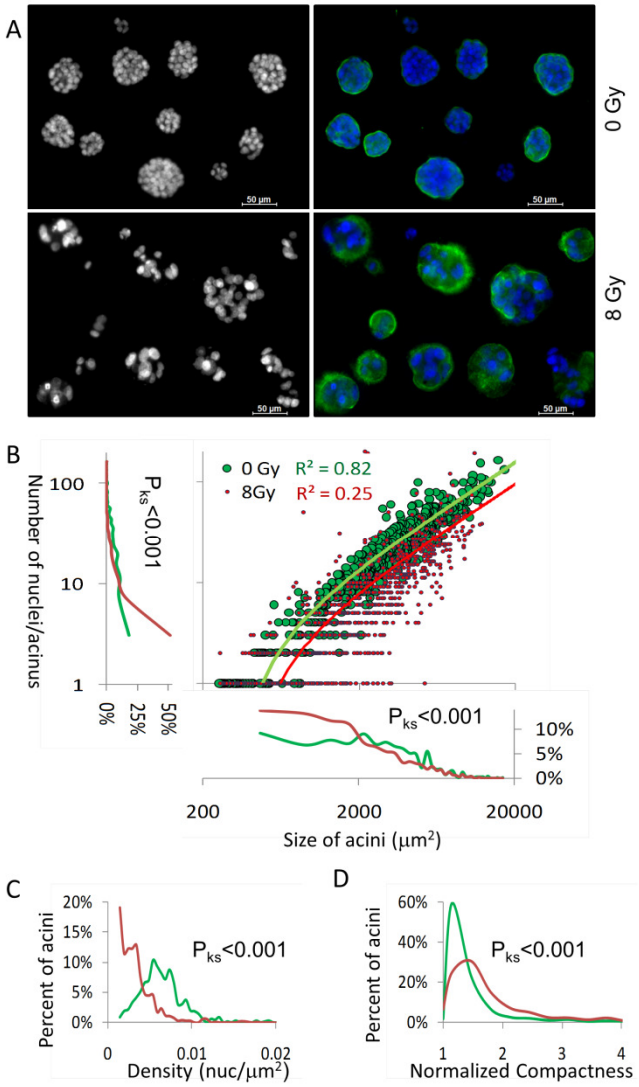

Fig. 2. Multi-dimensional characterization using high-content image analysis distinguishes 8Gy irradiated and non-irradiated populations in 3D lrECM. (A) Image of DAPI nuclei and α6 integrin immunoflourescece are shown from a 400 µm x 300 µm montage of MCF10A colonies +/- 8 Gy IR from 3D lrECM. Images were acquired with a 20X objective. (B) The number of nuclei per acinus is plotted against the acinar volume (log-log scale) N=1000 acini per treatment, 0 Gy=large green circles, 8 Gy=small red circles. Linear regression shows high correlation between these two measurements (linear regression indicated by solid lines, with corresponding R^2 values for both fits). Histograms for each parameter are plotted for nuclei/acinus on the left, Ks-test; P<0.001) and size of acini below, Ks-test; P <0.001. (C) Distributions for nuclear density measured per acinus shows significantly higher nuclear density in the 0 Gy vs. 8 Gy exposed populations, Ks-test showing P_{ks}<0.001. (D) Compactness analysis shows that sham treated acini (green curve) were more spherical with a narrow distribution close to 1 (value for a perfect circle), compared to the 8 Gy treated group showing more deformed acini (red curve); Ks-test, P_{ks}<0.001.

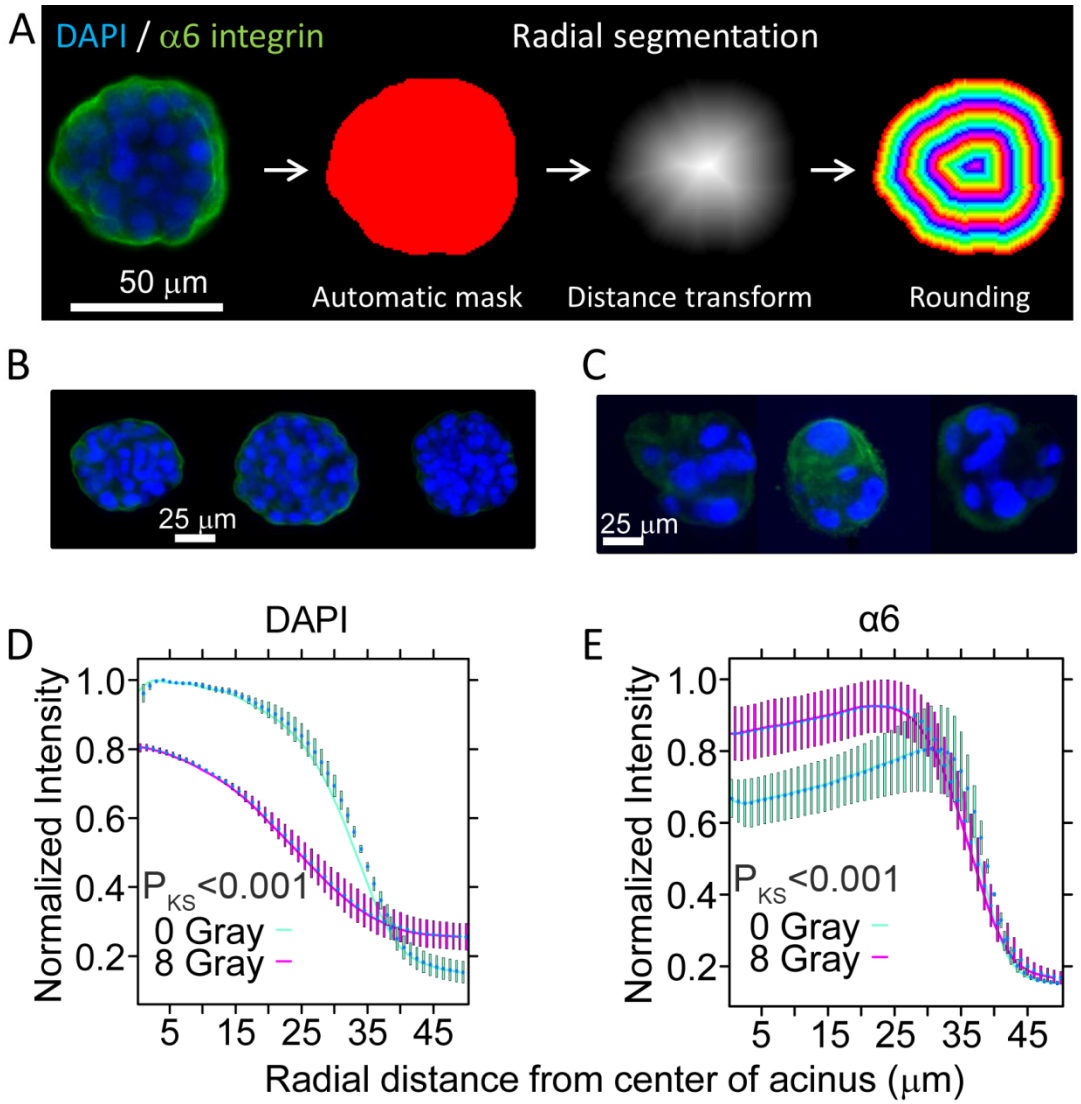

Fig. 3. Average concentric radial intensity profiles reveal redistribution of α6 integrin and DAPI signals in irradiated compared to non-irradiated MCF10A populations in 3D lrECM. (A) A single non-malignant untreated MCF 10A acinus in 3D lrECM immunostained for α6 integrin (green) and DAPI (blue) is shown. Automated acinus contour and concentric rings were determined to compute the average 1D radial intensity profile for each fluorochrome channel (B-C). Acini of the same size were considered for both groups and representative images are shown for 0 Gy and 8 Gy group respectively. (D) The lower nuclear density in the 8 Gy group can also be visualized easily with radial profiles showing a significant drop in the level of DAPI inside the acinus, compared to a much more dense nuclear occupation for 0 Gy. (N=3 experiments, hundreds of acini per experiment, K–S test) (E) Composite radial profiles of α6 integrin intensity show that for control MCF10A acini, α6 immunofluorescence is predominantly located at the surface of the acini; in contrast, α6 immunofluorescence distribution is flatter across the full acinus and more intense in the 8 Gy treated group, indicating a loss of polarization (N=3 experiments, hundreds of acini per experiment, K–S test).

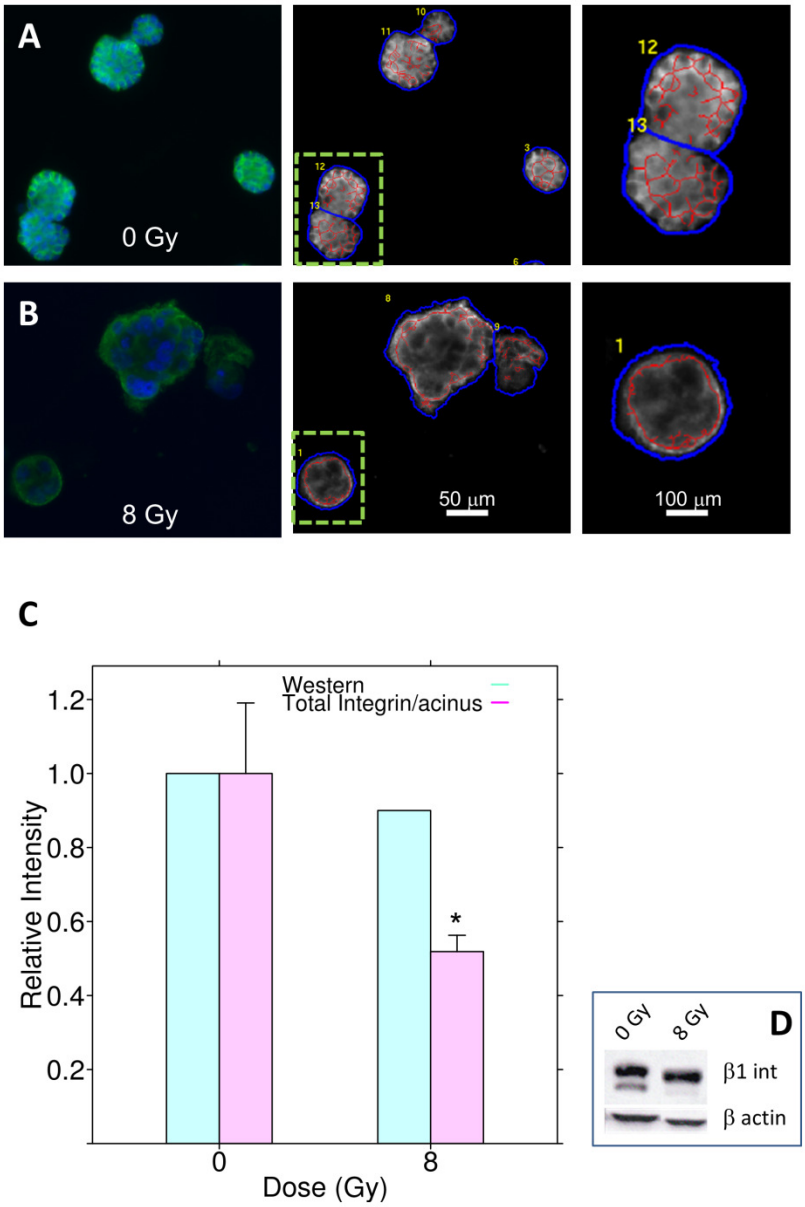

Fig. 4. Skeletonization of β1 integrin allows measurement of signal at cell-cell contact points. (A) Representative images of Sham treated MCF-10A acini, with intercellular β1 integrin intensity distribution. Middle panel shows the processed image, with skeletonization of β1 integrin signal. A region of interest is shown by green dashed lines and in high power in the right panel. (B) Similarly, representative images and processed images are shown for the 8 Gy treatment. (C) Skeletonization (magenta bars) indicates a 50% loss of β1 integrin at cell-cell interfaces in the 8 Gy population, (Wilcoxon rank-sum test. N=4 experiments, $P<0.05$). In contrast, western blots show a modest overall decrease (10% drop), bars in aquamarine=β1 integrin per β-actin. (D) Western blot used for quantification in panel C.

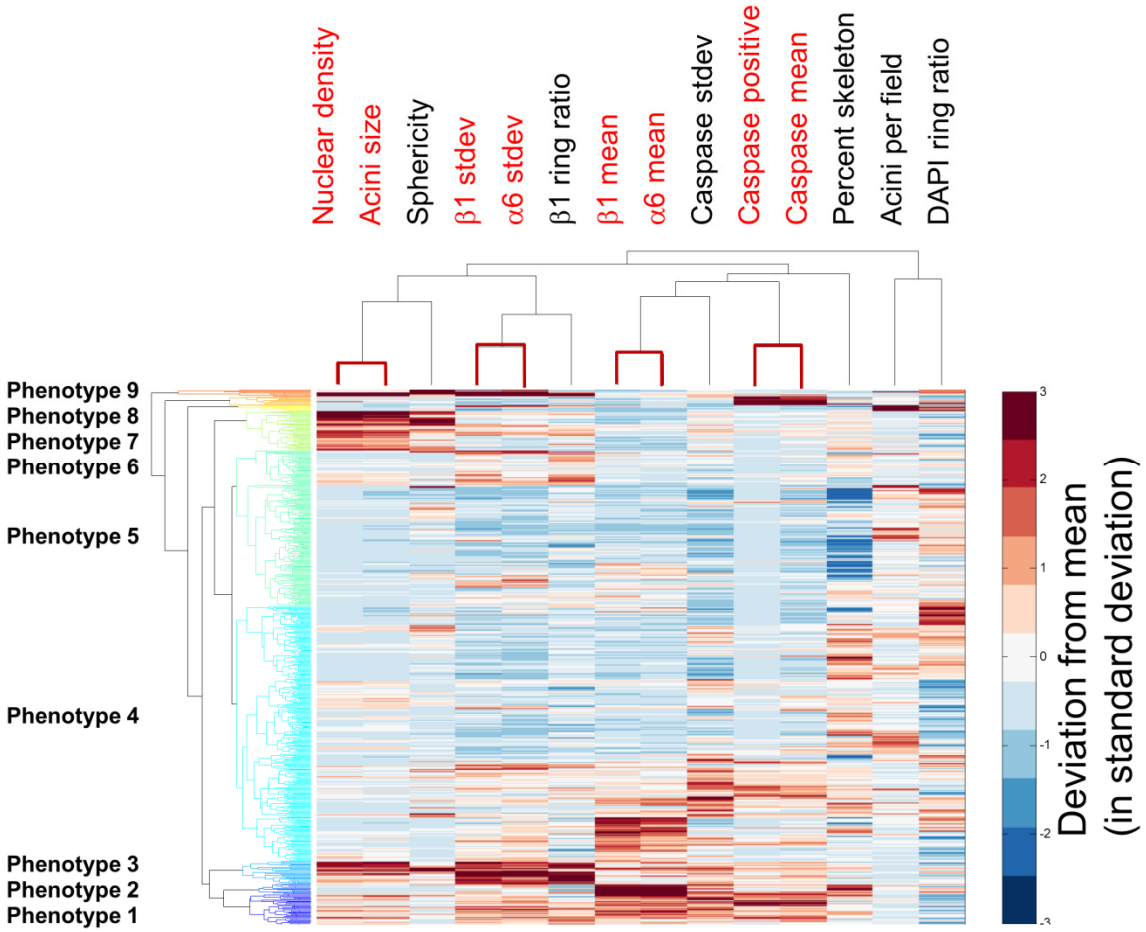

Fig. 5. Hierarchical clustering of imaging features identify 9 main phenotypes
Fourteen imaging features were used to characterize more than 1000 acini from four different treatments (T4, T4+IR, T4+A2B2, T4+A2B2+IR). Both features and acini profiles are classified using hierarchical clustering based on Pearson correlation. This approach reveals nine predominant phenotypes, which are present across all treatments.

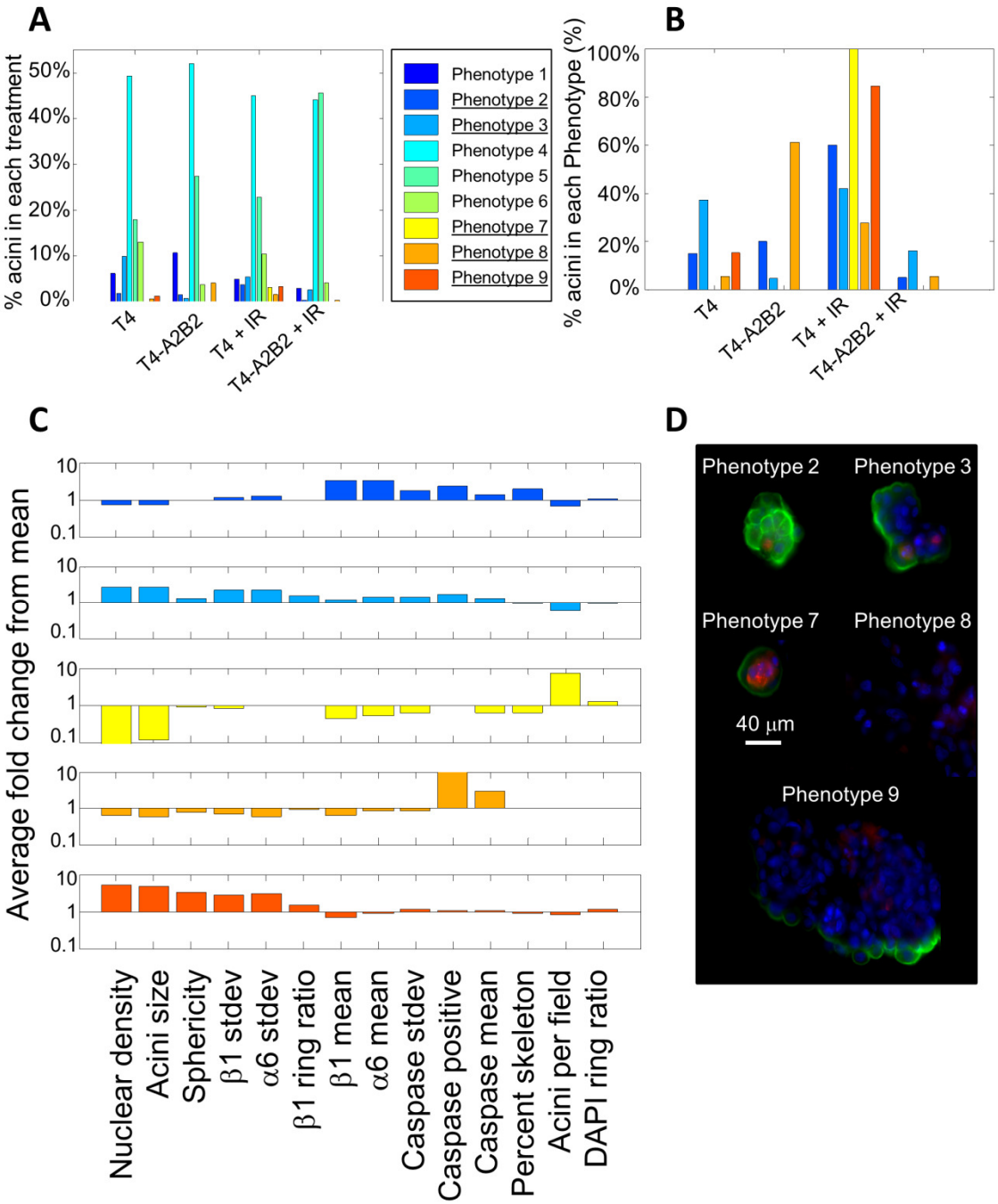

Fig. 6. Identification of five phenotypes enriched in the four different treatment groups. (A). For each treatment (T4, T4+IR, T4+AIIB2, T4+AIIB2+IR), the proportion of acini having each of the nine phenotypes is reported. (B) Five phenotypes with strong differential distribution between the four treatment groups were identified. (C) Signatures of the five phenotypes are illustrated by the average fold change for each feature over the mean across all acini. (D) Representative images are shown for each of the 5 specific phenotypes (blue:DAPI, green: β1-integrin, red: caspase).

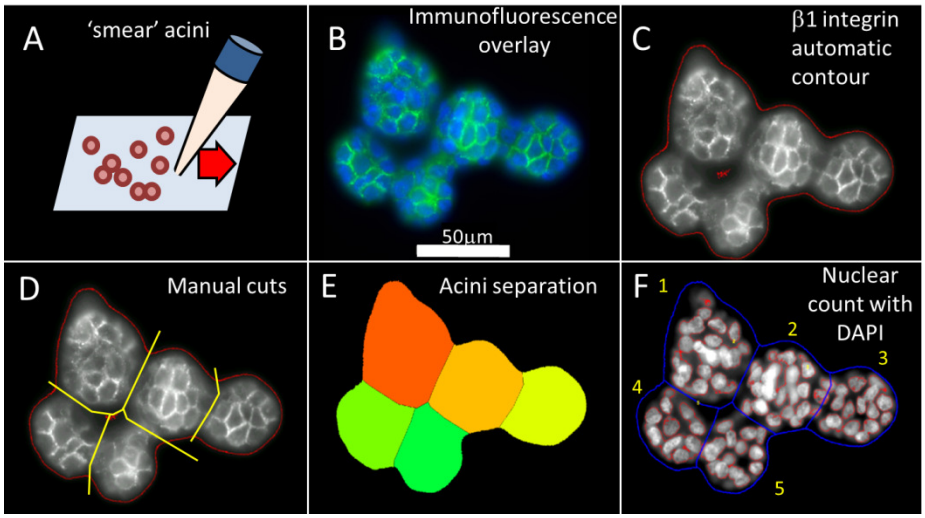

Supplemental Fig. S1. Sample preparation. (A) To perform immunofluorescence on nonmalignant immortalized human breast cells MCF 10A grown in 3DlrECM, we gently smeared the Matrigel™ onto treated glass slides. (B) Example of immunostaining of acini (DAPI for nuclear staining (blue), β1 integrin staining in green). Note that this technique does not disaggregate clustered acini. (C) Integrin immunofluorescence can be used to delimit the main contour of the acini using automatic thresholding. (D) Acini are separated manually by drawing internal contour lines. (E) Resulting labeled contours are shown (each color represents a separate acinus). (F) Individual acini are then delimited and nuclear counts are performed.

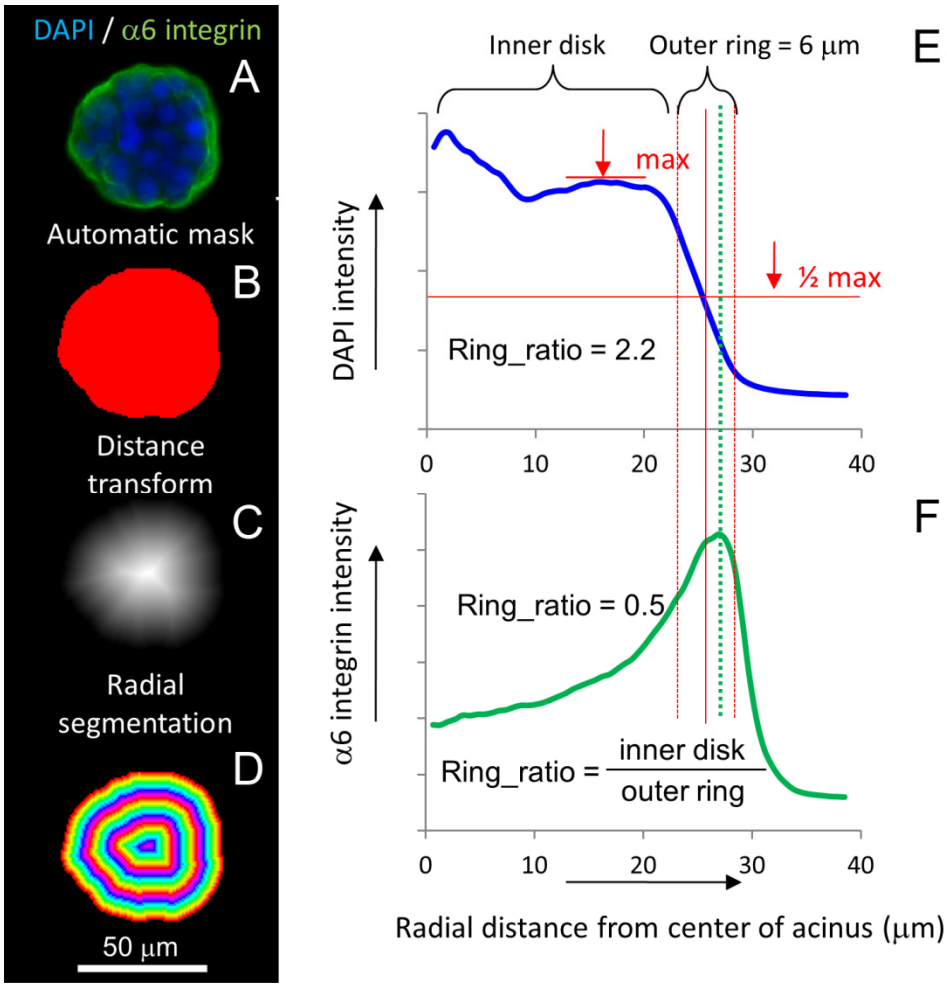

Supplemental Fig. S2. Expanding concentric and volumetric analysis (average concentric radial intensity (ACRI) profiles) characterizes spatial localization of integrins within each acinar structure. (A). Normal MCF 10A acinus in 3D lrECM immunostained for α6 integrin (green) and DAPI (blue) is shown. (B) Automated acinus contour based on isodata thresholding, holes filling and binary dilation to have a contour ~10 μm larger than the acinus contour. We then compute the distance transform of this mask (C) and round it to obtain a series of concentric layers (D) which are then used to compute the mean intensity of the protein in each layer (α6 integrin in this case, in green). This allows computation of a radial volumetric signal intensity profile from the geometric center of the acinus. (E) Radial profile of DAPI signal intensity for acinus shown in (A). For a simpler metric, one can define an outer ring as a ring centered on the acinus boundary (red solid vertical line) of thickness 6 μm (empiric value that typically include the basement membrane for a normal acinus). Outer ring as well as the inner disk inside the acinus are used to compute the ring_ratio as the mean intensity in the inner disk divided by the mean intensity in the outer ring. This leads to a value of 2.2 for DAPI, illustrating the fact that DAPI is predominantly inside the acinus. (F) Radial profile for α6 integrin for acinus shown in (A). The boundary of basement membrane is located at the peak of this profile (green dotted line). The ring_ratio for α6 is 0.5, illustrating the fact that the basement membrane lies within the outer ring.

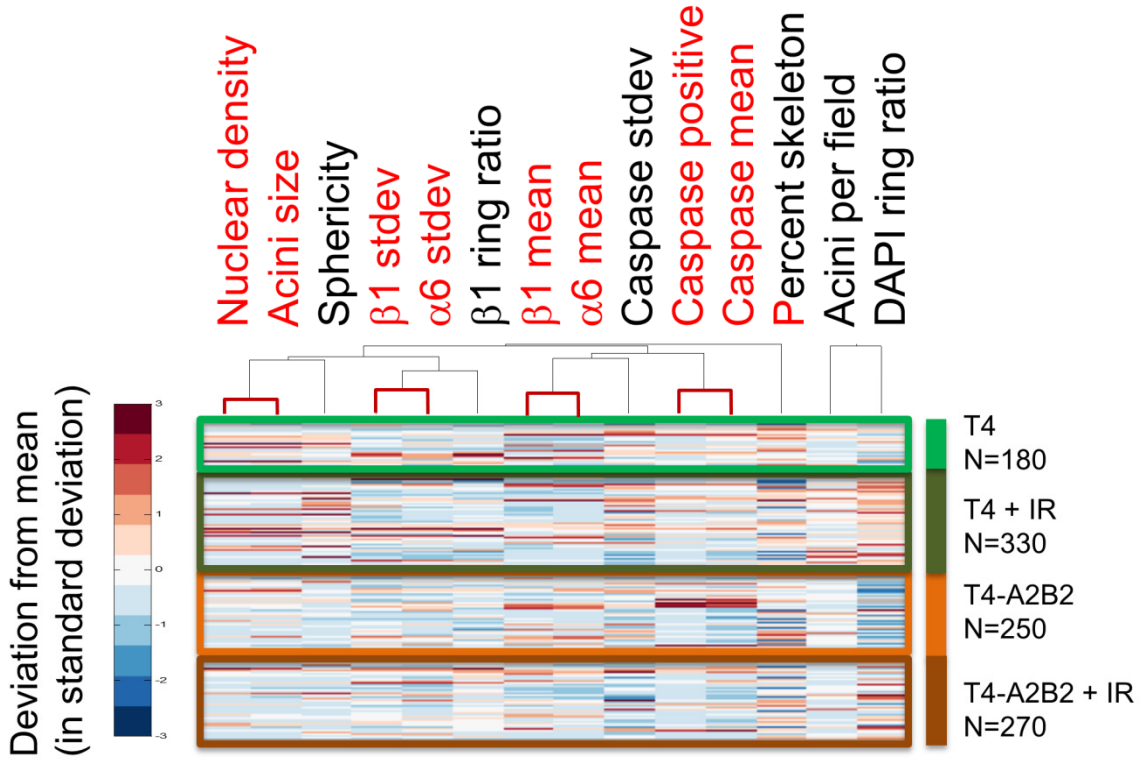

Supplemental Fig. S3. Highly correlated imaging features. 14 imaging features were used to characterize more than 1000 acini from four different treatments (T4, T4+IR, T4+A2B2, T4+A2B2+IR). Hierarchical clustering was based on Pearson correlation and only applied to identify imaging features that are highly correlated across all specimens (features shown in red). We find that the size and the number of nuclei per acinus are within the same feature cluster. Both α6 and β1 integrin immunostaining also reveal highly correlated features. Finally, looking at cell death either by total amount of Caspase per acinus or by counting the number of positive cells with caspase leads to similar values. However, when looking across acini (rows), no clear difference can be observed between the four treatments.

DISCLAIMER

This document was prepared as an account of work sponsored by the United States Government. While this document is believed to contain correct information, neither the United States Government nor any agency thereof, nor the Regents of the University of California, nor any of their employees, makes any warranty, express or implied, or assumes any legal responsibility for the accuracy, completeness, or usefulness of any information, apparatus, product, or process disclosed, or represents that its use would not infringe privately owned rights. Reference herein to any specific commercial product, process, or service by its trade name, trademark, manufacturer, or otherwise, does not necessarily constitute or imply its endorsement, recommendation, or favoring by the United States Government or any agency thereof, or the Regents of the University of California. The views and opinions of authors expressed herein do not necessarily state or reflect those of the United States Government or any agency thereof or the Regents of the University of California.

DE-AC02-05CH11231